

RESEARCH ON AN AERODYNAMIC LOAD METHODOLOGY FOR FLAPPING WINGS BASED ON EXPERIMENTALLY ACQUIRED DEFORMATION

Kairong Yang[1,2], Bifeng Song[1,2], Dong Xue[1,2]

[1]School of Aeronautics, Northwestern Polytechnical University, Xi'an 710072, China

[2]National Key Laboratory of Aircraft Configuration Design, Xi'an 710072, China

Abstract

Compared with traditional fixed-wing aircraft, flapping-wing micro aerial vehicle is often used for reconnaissance missions in narrow and complex terrains such as densely populated high-rise buildings due to their superior concealment, high maneuverability, and greater propulsion efficiency at low Reynolds number. They can be widely used in military and civilian fields, making them one of the current hot issues in the field of biomimetics. Among bird-like flapping-wing aircrafts, wings are the most crucial component for generating lift and thrust. Therefore, this paper focuses on studying the aerodynamic characteristics of the flapping wing of ‘Dove’. During actual flapping, significant deformations occur in the flapping wing, which significantly influences its aerodynamic characteristics. Meanwhile, it is not feasible to directly measure the aerodynamic force of the flapping wing during the experiment. This paper utilizes high-speed Photogrammetry to investigate the dynamic deformation measurement method of the flexible flapping wing of ‘Dove’. By coupling the DIC-measured deformation with the CFD method, a CFD approach that considers flexible deformation is established. Based on this method, the aerodynamic characteristics of the flexible flapping wing of ‘Dove’ under the same experimental conditions are studied. The comparative results reveal that the lift generated by the flexible wing is lower than that of the rigid wing, while the thrust generated by the flexible wing is significantly higher. This indicates that flexible deformation has a significant impact on the aerodynamic characteristics of the flapping wing, which merits further exploration. The development of a calculation method for simulating the dynamic deformation of the flapping wing of ‘Dove’ is of great significance for analyzing its aerodynamic characteristics.

Keywords: flapping-wing micro aerial vehicle; CFD; photogrammetry; aerodynamic force calculation

1. Introduction

Compared with conventional fixed-wing aircraft, bird-inspired flapping-wing air vehicles have become a focal topic in bionics research owing to their superior stealth, high maneuverability, and higher propulsive efficiency at low Reynolds numbers [1-4]. Theoretical investigations indicate that the aerodynamic efficiency of flapping wings exceeds that of conventional fixed wings [5-7]. In a bird-mimicking flapping system, the wing is the primary component responsible for lift and thrust generation; consequently, accurate prediction of the aerodynamic loads on such wings constitutes one of the most challenging problems in flapping-wing aerodynamics.

During actual flapping motion, the wing undergoes pronounced deformation, and this dynamic flexibility exerts a decisive influence on aerodynamic characteristics. Moreover, the aerodynamic forces acting on a flapping wing cannot be directly measured in wind-tunnel experiments. To accurately calculate the aerodynamic loads on a bird-inspired flapping wing, it is necessary to introduce Computational Fluid Dynamics (CFD) and Computational Structural Dynamics (CSD) methods into the aerodynamic analysis, constructing a CFD/CSD coupling method. When CFD/CSD coupling is employed to compute the aerodynamic loads of bird-inspired wings, two major obstacles arise: (1) difficulties in establishing an accurate structural model and (2) the requirement for robust

mesh-deformation capability during CFD computation.
Currently, extensive research has been conducted both domestically and internationally on the aerodynamic characteristics of dynamic flexible deformation of bird-inspired flapping wings. Dynamic flexible deformation significantly affects the thrust, lift, and power consumption of the wing. Bird wings exhibit significant flexible deformation during flapping [8]. Heathcote et al. [9-10] found through water tunnel experiments that appropriate chordwise or spanwise flexibility can increase thrust coefficient and propulsive efficiency, but excessive flexibility leads to performance degradation. Deng et al. [11] used three-dimensional stereo vision measurement combined with an overset mesh method to achieve numerical simulation of a flexible flapping wing. Through comparison, they found that the numerical results were basically consistent with the experimental results, validating the method as correct and effective, and providing new ideas and methods for flexible flapping wing research. Song et al. [12-13] conducted three-dimensional numerical simulations on the hovering flight of a ruby-throated hummingbird, using real wing kinematic data reconstructed via a high-speed camera system. Bode-Oke et al. [14] used a similar method to study the aerodynamic characteristics of a monarch butterfly in backward flight. Shumway et al. [15] investigated the effect of dragonfly wing deformation on its forward flight aerodynamic performance, among others.
The team of Professor Bifeng Song at Northwestern Polytechnical University has also conducted a series of studies on the impact of dynamic flexible deformation of flapping wings [16-18]. The team developed a series of CFD/CSD coupling solvers to study the effect of flexible deformation on the aerodynamic characteristics of micro flapping wings. For the 'Dove'-inspired wing, Xiaowu Yang [18] researched aerodynamic force calculation and inertial force calculation methods for flexible wings based on measured deformation, finding that simulation results based on measured deformation agreed well with experimental results.
Against this background, the present research is based on the 'Dove'-inspired wing. To circumvent these issues, the present study adopts an emerging approach that integrates CFD with full-field deformation data obtained by high-speed stereo digital image correlation (DIC). Replacing the conventional CSD module with experimentally measured deformation data eliminates the need for structural modeling. By coupling the experimentally acquired deformation field with a rigid-wing CFD solver, a flexibility-incorporated CFD methodology is established, enabling aerodynamic analysis of a flexible “Dove” wing under conditions identical to those of the experiment. By contrasting the aerodynamic behavior of rigid and flexible configurations, the underlying mechanisms through which flexibility affects the aerodynamic performance of dove-inspired wings are explored, laying the foundation for uncovering the aerodynamic rationale of flexible flapping wings.

2. Numerical Methods and Validation

The core of Computational Fluid Dynamics (CFD) involves solving the governing equations of fluid dynamics by applying various numerical discretization methods via computer technology. Therefore, the fundamental governing equations of fluid dynamics constitute the theoretical foundation of this discipline. These equations primarily include the continuity equation, the momentum equation, and the energy equation. Since the research object of this paper is the 'Dove'-inspired flapping wing, which typically flies at very low speeds, the governing equations can be further simplified to those for incompressible flow. Thus, the continuity equation simplifies to:

$$\nabla \cdot \vec{V} = 0 \tag{1}$$

The momentum equation is expressed as:

$$\frac{\partial}{\partial t}(\rho \vec{v}) + \nabla \cdot (\rho \vec{v}\vec{v}) = -\nabla P + \nabla \cdot (\bar{\bar{\tau}}) \tag{2}$$

where ρ is the fluid density, $\vec{v}$ is the velocity vector, P is the static pressure, and $\bar{\bar{\tau}}$ is the stress tensor. Here, $\bar{\bar{\tau}}$ is expressed as:

$$\bar{\bar{\tau}} = \mu\left[(\nabla \vec{v} + \nabla \vec{v}^T) - \frac{2}{3}\nabla \cdot \vec{v} I\right] \tag{3}$$

where μ is the dynamic viscosity and I is the unit tensor. The energy equation is expressed as:

$$\frac{\partial(\rho T)}{\partial t} + div(\rho u T) = div\left(\frac{\kappa}{c_P} grad T\right) + S_T \quad (4)$$

This equation uses temperature T as the variable. Here, c_P is the specific heat capacity, T is the temperature, κ is the thermal conductivity, and S_T is the energy converted from viscous effects within the fluid, i.e., the viscous dissipation term. For incompressible flow, the energy equation can often be neglected.

2.1 Geometric Model and Mesh Generation

The model was established based on the original pigeon wing from the Bionic Flight Vehicle Research Group of Northwestern Polytechnical University, as shown in Figure 1. The chord length at the wing root is 100 mm, the semi-span is 290 mm, and the thickness is 1.5 mm.

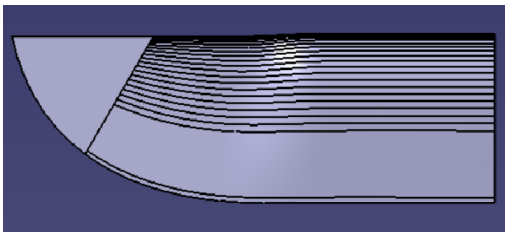
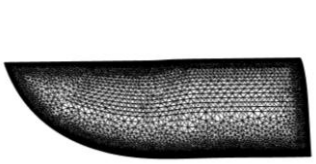
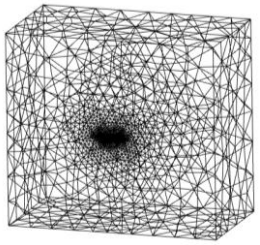


Figure 1 – 'Dove' rigid wing modeling.

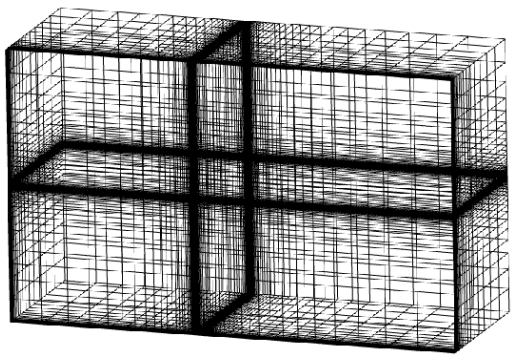
Subsequently, meshing was performed for each sub-module. Figure 2 shows the overset grid system for the pigeon wing. The grid system consists of three parts: the surface mesh, the component mesh, and the background mesh. The background mesh uses a structured grid, the component mesh uses an unstructured grid composed of tetrahedral elements, the wing surface mesh uses triangular elements, and the boundary layer mesh consists of prism layers extruding outward from the surface mesh. The component mesh is embedded within the background mesh and follows the rotational motion of the flapping wing, deforming internally as the wing deforms. The background mesh is refined in the region embedding the component mesh to ensure similar grid sizes near the interface for accurate data transfer.



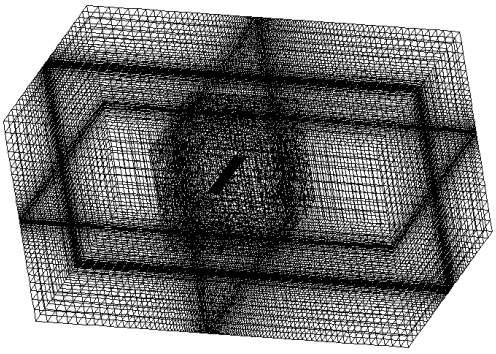
(a)Surface mesh



(b)Component mesh



(c)Background mesh



(d)Overall mesh

Figure 2 – Overall overset mesh for the 'Dove' rigid wing.

2.2 Numerical Methods and Boundary Conditions

After constructing the overset grid system, it was imported into Fluent to set boundary conditions and other parameters. The inlet was set as a velocity inlet boundary condition, the outlet as a pressure outlet boundary condition (101325 Pa). Since the model is a half-span simulation, the symmetry plane was set as a symmetry boundary condition. The component grid boundary was set as an overset boundary condition, and the wing surface was set as a no-slip wall boundary condition. The turbulence model used was the $k-\omega$ SST model. The numerical method employed the coupled algorithm. The gradient interpolation method was Least Squares Cell Based. Second-order discretization schemes were used for pressure and momentum, and a first-order implicit scheme was used for temporal discretization.

2.3 Kinematic Model

The rigid wing motion used a pure flapping (plunging) kinematic model, expressed as:

$$\psi(t) = \psi_0 \sin(2\pi f t) \tag{5}$$

where ψ_0 is the flapping amplitude and f is the flapping frequency.

2.4 Method Validation and Grid Independence Study

This paper uses Fluent's overset mesh method with a User-Defined Function (UDF) to implement the flapping motion of the wing. To validate that this method can effectively and accurately calculate the aerodynamic characteristics of flapping wings, the water tunnel experiment of Heathcote [10] (2008) was used as a reference, and the same parameters were set for simulation. The calculation results were compared with the experimental data of Heathcote [10], the computational results of Hao Liu [19], and the computational results of Lang Xinyu [20], as shown in Figure 3. It can be seen that the peak values of the thrust coefficient differ slightly, but the phase is very close, agreeing well with Lang's results, thus validating the accuracy of the present method.

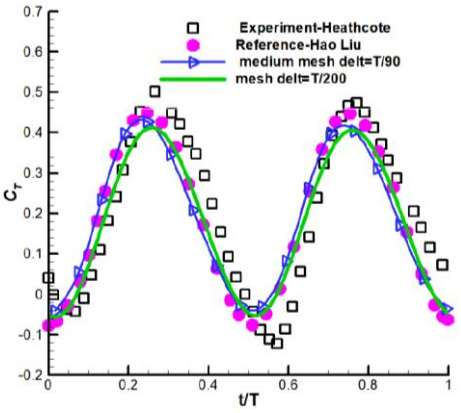


Figure 3 – Comparison of thrust coefficient with experimental and numerical results.

Subsequently, a time-step independence study was conducted. Time steps of T/120, T/200, and T/320 were used with a total mesh count of 2.11 million (1.82 million for component mesh, 0.29 million for background mesh). The results are shown in Figure 4. The lift and drag for the three time steps are basically consistent, and the error between T/200 and T/320 is significantly smaller than that between T/120 and T/200, indicating convergence. Therefore, a time step of T/200 was used for subsequent calculations.

Next, a grid independence study was performed. Three sets of grids with approximately 1.3 million, 2.11 million, and 3.5 million cells were selected for calculation with a time step of T/200. The grid counts for the three sets are shown in Table 1, and the result comparison is shown in Figure 5. The lift trends, peaks, and phases for the three grids are quite similar. Therefore, the grid with 2.11 million cells was used for subsequent comparison with experiments.

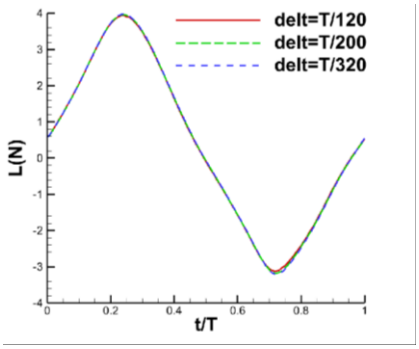


Figure 4 – Time-step independence study.

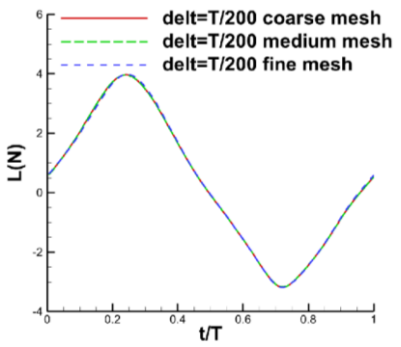


Figure 5 – Grid independence study.

Table 1 – Three different mesh sizes.

Mesh Set	coarse mesh	medium mesh	fine mesh
Total Mesh(millions)	1.30	2.11	3.50
Component Mesh(millions)	1.02	1.82	3.20
Background Mesh(millions)	0.28	0.29	0.30

3. Aerodynamic and Inertial Force Calculation Method for Flexible Wing Based on DIC-Measured Deformation

3.1 DIC Dynamic Deformation Measurement System and Principle

To capture the real flexible deformation of the flapping wing, this paper adopts the photogrammetry method. The Digital Image Correlation (DIC) system uses two cameras to construct a stereo vision system simulating human binocular vision, enabling spatial image acquisition of objects and achieving positioning through advanced image processing algorithms.

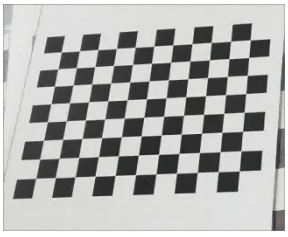
The DIC system mainly includes: two high-speed cameras (up to 800 fps at 2560×1600 resolution), three high-brightness fill lights, a checkerboard ceramic calibration plate (12×9 squares, 20 mm side length), a data communication module, and data processing software, as shown in Figure 6.



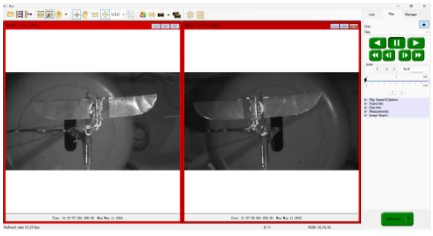
(a)Phantom VEO-E 340L high-speed camera



(b)LED-2000 high-brightness fill light



(c)Calibration board and marker distribution



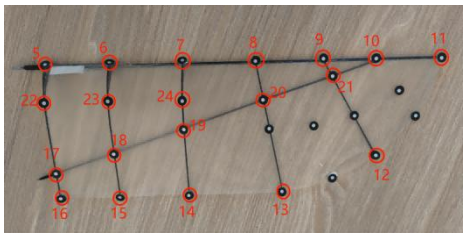
(d)Data processing software

Figure 6 – DIC dynamic deformation measurement system.

To reconstruct the wing surface and transform coordinates from the measurement frame to the body frame of the flapping mechanism, two types of markers are needed: markers for surface

reconstruction and markers for coordinate transformation. As shown in Figure 7(a), 20 markers were placed on the wing, all on the carbon fiber rods (leading edge rod, diagonal rod, and rib intersections – points 5 to 21). Three additional markers (points 22, 23, 24) were placed at the maximum camber of the ribs to simulate rib curvature more accurately.

As shown in Figure 7(b), four points were marked for coordinate transformation, defining the body coordinate system. The vector from point 1 to point 2 defines the x-direction of the flapping mechanism's body frame. The vector from point 3 to point 4 defines the y-direction. The z-direction is obtained by the cross product of the x and y vectors. The origin of the body coordinate system is set at point 1.



(a)Markers for wing membrane reconstruction

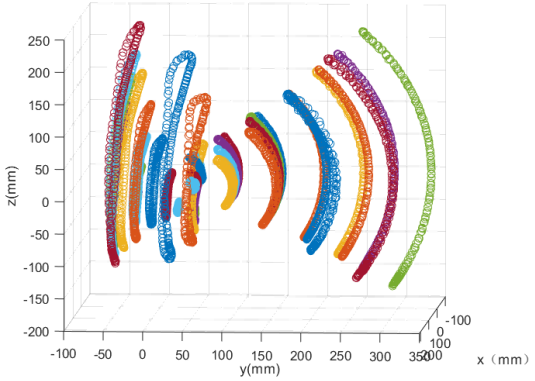


(b)Markers for coordinate transformation

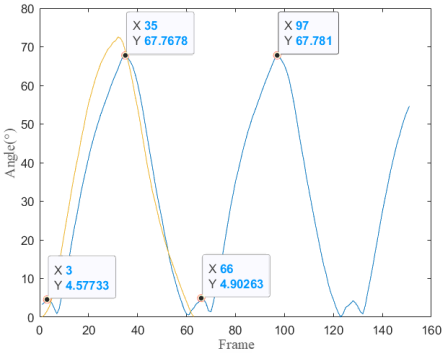
Figure 7 – Arrangement of markers on the flapping wing.

3.2 Experimental Data Processing

After image acquisition, the DLTdv8 software was used to process the image data. To ensure high accuracy, manual identification was used throughout. Next, coordinate transformation was performed to convert coordinates from the measurement frame to the body frame defined by the mechanism markers (Figure 8). After transformation, the leading edge vector at a randomly selected time was used to calculate the angle with leading edge vectors at all other times, obtaining the periodic variation of the flapping angle. Combined with the camera timing information, frames 35 to 97 were determined as one complete flapping cycle, yielding a flapping angle of approximately 72° .



(a)Marker position change before and after transformation



(b)Determination of flapping angle and cycle coordinates

Figure 8 – Marker positions before and after coordinate transformation and determination of flapping angle and complete cycle.

After obtaining the coordinates for a complete cycle, data fitting was used to obtain analytical expressions for the marker coordinate components as functions of time. This removes data with large fluctuations, smoothing the data model. An 8th-order Fourier series was used for fitting the marker coordinate data. Figure 9 shows the continuous variation of marker coordinates over time after Fourier fitting.

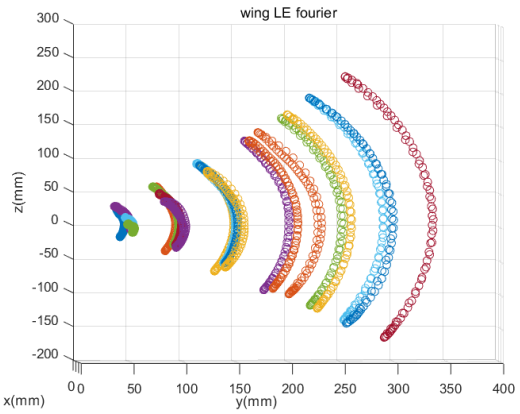
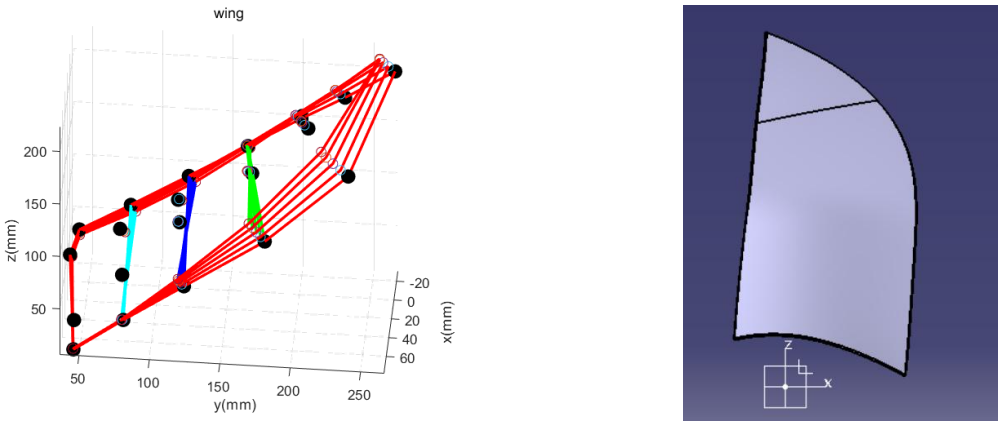


Figure 9 –Fitted marker coordinates after Fourier series fitting.

3.3 Flexible Wing Surface Reconstruction and Mesh Generation

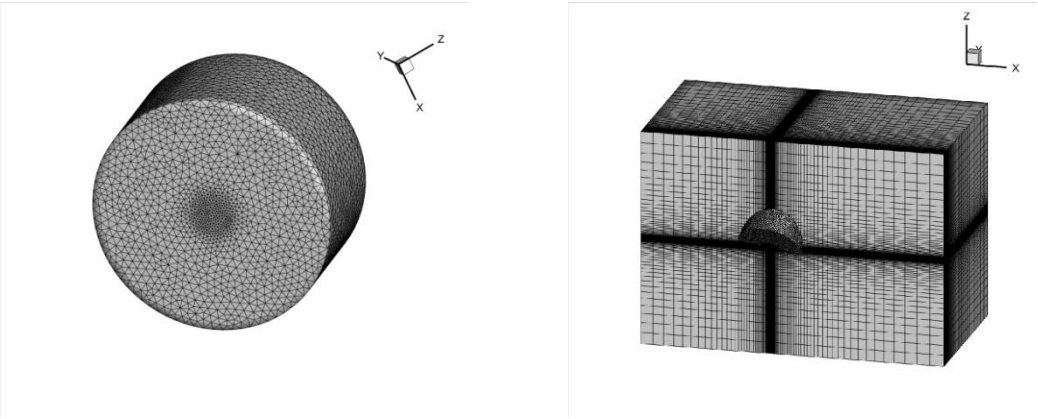
For CFD calculation, the flapping wing surface needed reconstruction based on the fitted marker data, followed by mesh generation. First, the initial time instant was determined. This should be a state with minimal wing deformation to avoid negative volumes during mesh generation. The upper flapping limit position was chosen as the initial time (Figure 10(a)), where deformation is minimal. A single-layer wing surface was reconstructed using multi-section and filled surface functions. Since the actual wing has a thickness of 1.5 mm, the reconstructed single-layer surface was slightly thickened to facilitate boundary layer mesh generation, resulting in a wing model with thickness (Figure 10(b)).



(a)Initial time marker coordinate determination (b)Reconstructed wing surface

Figure 10 – Determination of initial time and reconstructed wing surface.

Subsequently, an overset mesh similar to the rigid wing case was generated, consisting of surface mesh, component mesh, and background mesh. The component mesh is embedded within the background mesh, follows the rotational motion of the flapping wing, and deforms internally. The component mesh count was approximately 1.02 million, and the background mesh count was approximately 0.92 million, as shown in Figure 11.



(a)Component mesh (b)Overall mesh

Figure 11 – Mesh generation for the flexible flapping wing.

3.4 Dynamic Mesh Deformation Method

Dynamic mesh deformation includes wing surface mesh deformation and volume mesh deformation. Surface mesh deformation is driven by the motion model of surface mesh nodes based on experimental measurements. Volume mesh deformation around the wing is achieved via smoothing methods.

For the flexible wing, the Radial Basis Function (RBF) method was used to transfer the surface mesh from the initial time to other time instants while preserving the mesh structure information, facilitating subsequent Fourier fitting of each mesh node's temporal variation. Boer et al. [21] first applied RBF to mesh deformation. The basic principle is interpolating known boundary node displacements using RBF, then using the constructed RBF series to smoothly assign the known boundary displacements to each unknown node.

Knowing the complete cycle coordinate data of all markers from experimental processing and the positions of initially generated surface mesh nodes, the RBF method interpolates the marker displacements at all time instants. The resulting RBF series smoothly assign the marker displacements to all surface mesh nodes, yielding surface mesh node coordinates at all sampled times. Next, Fourier fitting is performed for each mesh node to obtain its motion model. The position of any surface mesh node at any time is determined based on the time variable, enabling continuous updating of the surface mesh with motion. Figure 12 shows the surface mesh (displayed as STL facet mesh) generated at different times based on RBF interpolation. This method yields a well-deformed wing surface mesh.

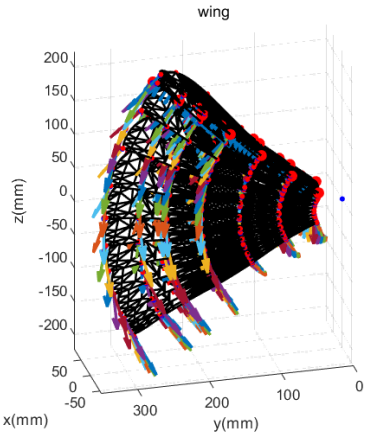


Figure 12 – Surface mesh deformation based on RBF interpolation at different time instants.

The deformation of the surface mesh must be transferred to the volume mesh via a suitable algorithm; i.e., the volume mesh must "absorb" the deformation of the surface mesh. Fluent includes three

volume mesh deformation algorithms: diffusion smoothing, spring smoothing, and linearly elastic solid smoothing. Spring smoothing is only suitable for simple deformations and has the weakest capability. Linearly elastic solid smoothing maintains better quality for some meshes but is computationally expensive. Diffusion smoothing, which offers strong deformation capability with lower computational cost, was chosen.

Finally, User-Defined Functions (UDFs) were used to implement mesh deformation and motion in Fluent to perform CFD calculations.

3.5 Inertial Force Calculation Method

During experiments, the balance measures the total force. By Newton's third law, the total force is the elastic restoring force of the wing. According to d'Alembert's principle, the elastic restoring force is the sum of the aerodynamic force and the inertial force of the flapping wing. Therefore, to validate the aerodynamic force calculation method described above, force measurement experiments were conducted under identical conditions. The vector sum of the aerodynamic force and inertial force was then compared with the experimentally measured force, using the validation formula:

$$F_{Exp} = F_{aero} + F_{inertial} \tag{6}$$

Several methods exist for calculating inertial force. This paper adopts the flapping wing discretization method. The wing membrane and frame constituting the flapping wing are discretized into elements. Using the experimentally obtained marker data and the material distribution properties of the membrane and frame, the inertial force of the discrete elements over a complete cycle is obtained. Integrating yields the total inertial force of the entire flapping wing over a complete cycle.

First, the wing membrane was discretized. Similar to the aerodynamic force calculation method, the membrane is treated as a surface without thickness and discretized using triangular mesh elements. For each discrete element, its inertial force is the product of the centroid acceleration of the mesh element and the element mass:

$$\Delta F_{film_iner} = \Delta m_{film} \cdot a(t) \tag{7}$$

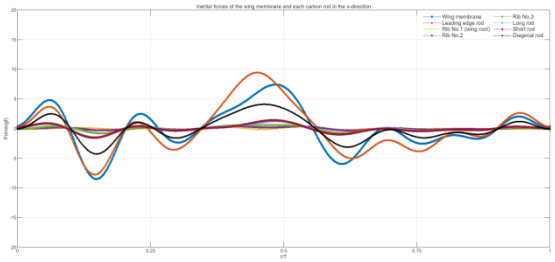
where $a(t)$ is the acceleration variation of the mesh element centroid, Δm_{film} is the mass of the membrane mesh element, and $\Delta m_{film} = \rho_{film} \cdot \Delta A_{film}$. Here, ρ_{film} is the membrane mass per unit area, and ΔA_{film} is the area of the membrane mesh element. To ensure node information transfer, RBF interpolation was used to obtain the temporal displacement function for all membrane mesh nodes. Differentiation yielded temporal velocity and acceleration functions. Summing the inertial forces of all mesh elements gave the total membrane inertial force.

Next, the frame was discretized. The frame consists of the leading edge rod, diagonal rod, three inner ribs, and outer section long and short rods. These rods were treated as spatial spline curves and discretized consistently with the membrane discretization nodes. For each discrete point, its inertial force is the product of its acceleration and its mass:

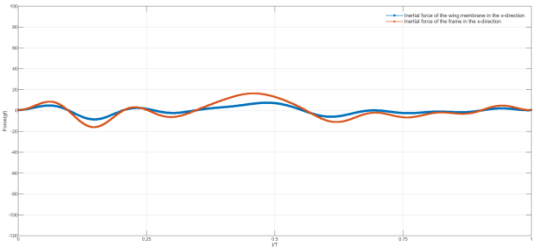
$$\Delta F_{rod_iner} = \Delta m_{rod} \cdot a(t) \tag{8}$$

where $a(t)$ is the acceleration variation of the point, Δm_{rod} is the mass of the rod discrete element, and $\Delta m_{rod} = \rho_{rod} \cdot \Delta S_{rod}$. Here, ρ_{rod} is the rod mass per unit length, and ΔS_{rod} is the distance between rod points. Similarly, RBF interpolation was used to obtain the temporal displacement function for all frame discrete points. Differentiation yielded velocity and acceleration functions. Summing the inertial forces of all points gave the total frame inertial force.

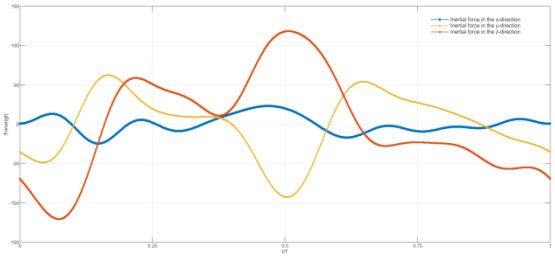
Under experimental conditions (freestream velocity 10 m/s, flapping frequency 8 Hz, rigid flapping amplitude 72°, angle of attack 8°), aerodynamic and inertial forces were calculated based on measured deformation data. Figure 13 shows the calculated inertial force components of the wing. The forces were then summed with the aerodynamic force to obtain the resultant forces in the three axes of the body frame.



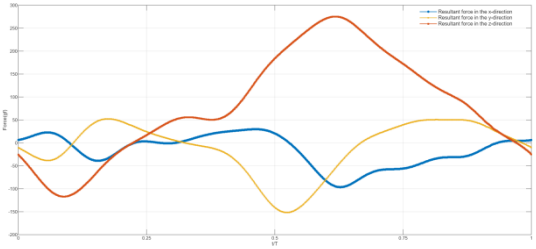
(a)Inertial force of membrane and rod components (x-direction)



(b)Inertial force of membrane and frame (x-direction)



(c) Inertial force in three directions



(d)Total inertial force in three directions

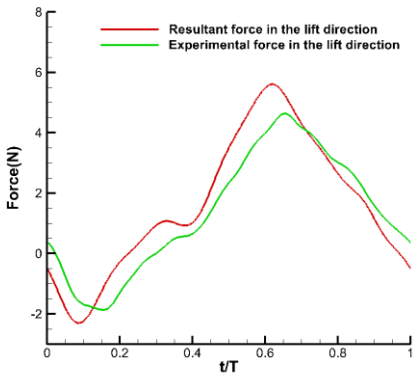
Figure 13 – Calculated inertial forces for the flexible wing.

The forces in the body frame were transformed to the wind axis system. The numerical results for the lift and thrust directions were extracted and compared with experimental data. Figure 14 shows the instantaneous comparison, and Table 2 shows the time-averaged force comparison. The trend of the resultant force from the numerical calculation agrees reasonably well with the experimental force in both lift and thrust directions. However, the experimental forces exhibit a slight phase lag, and a larger peak difference appears at the initial moment in the thrust direction. Potential error sources are inferred as follows:

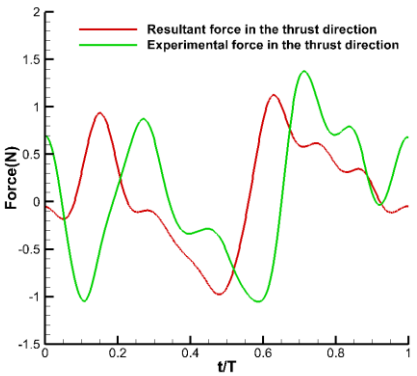
1. In the DIC-based deformation measurement experiment, the frame rate might have been insufficient to precisely capture the upper and lower flapping limits, introducing phase errors when extracting the complete flapping cycle.

2. The measured deformation data requires interpolation and fitting, which may amplify errors in the deformation data and its derivatives at peak moments, leading to larger deviations at those peaks.

Overall, the forces calculated using the method incorporating measured deformation show good agreement in trend and peak values. For aerodynamic mechanism analysis, small phase differences have a limited impact on comparing rigid and flexible wing aerodynamics. This validates the rationality and effectiveness of the DIC-based dynamic deformation measurement technique. This validation is the critical prerequisite for subsequent aerodynamic load computations incorporating measured deformation.



(a)Lift direction comparison



(b)Thrust direction comparison

Figure 14 – Comparison of numerical resultant force and experimental force under identical conditions.

Table 2 – Comparison of time-averaged forces from numerical calculation and experiment under identical conditions.

Force Type	The time-averaged force in the lift direction	The time-averaged force in the thrust direction
Numerical Resultant Force(N)	1.606	0.102
Experimental Force(N)	1.343	0.075

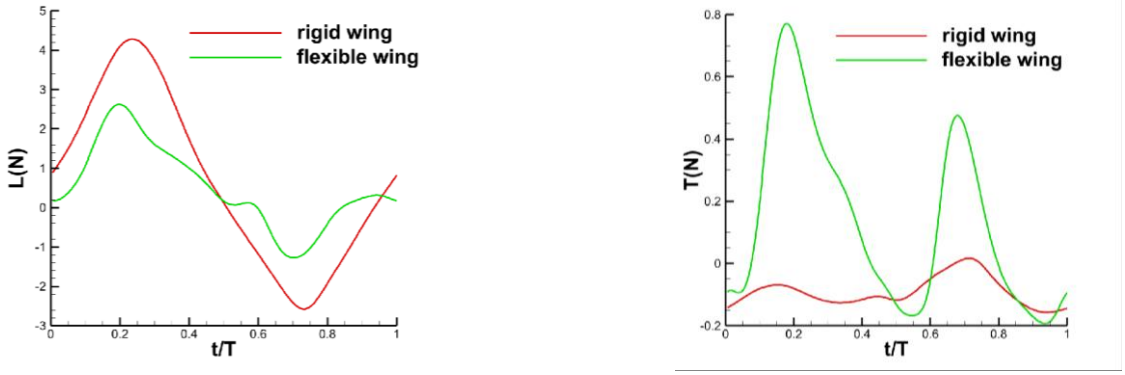
4. Comparison of Aerodynamic Characteristics Between Rigid and Flexible Wings

Aerodynamic force calculations were performed for both the rigid wing and the flexible wing (based on measured deformation) under experimental conditions (freestream velocity 10 m/s, flapping frequency 8 Hz, rigid flapping amplitude 72°, angle of attack 4°).

4.1 Comparison of Lift and Thrust Characteristics

Figure 15(a) shows the instantaneous lift comparison between the rigid and flexible wings over one cycle. The lift trends of the two wings are generally similar, both showing a distinct peak (downstroke) and trough (upstroke). For the rigid wing, the lift peak and trough occur near the times of maximum downstroke velocity (t/T=0.25) and maximum upstroke velocity (t/T=0.75). For the flexible wing, the times for reaching the lift peak and trough are slightly advanced. Near the downstroke limit position (t/T=0.5), unlike the rigid wing whose instantaneous lift continuously decreases, the flexible wing's instantaneous lift shows a plateau or even a slight increase before starting to decrease. This phenomenon indicates that flexible deformation delays lift loss near the downstroke limit to some extent. Furthermore, the peak instantaneous lift of the flexible wing is noticeably lower than that of the rigid wing, while its lift trough is higher than that of the rigid wing. Comparing time-averaged lift, as shown in Table 3, the flexible wing's time-averaged lift is lower than that of the rigid wing.

Figure 15(b) shows the instantaneous thrust comparison between the rigid and flexible wings over one cycle. The difference in thrust characteristics between the rigid and flexible wings is far more significant than for lift. For the rigid wing, during the downstroke, two peaks (one large, one small) appear successively, but thrust remains negative throughout this phase. During the upstroke, a single larger peak occurs, with the thrust peak appearing near the time of maximum upstroke velocity (t/T=0.75), and the peak value is a small positive number. The flexible wing's thrust curve is completely different. During both downstroke and upstroke, a large thrust peak appears, with both peaks being large positive values, occurring approximately at t/T=0.2 and t/T=0.7, slightly advanced, and the downstroke peak is significantly higher than the upstroke peak. Observing the thrust peaks and troughs of the two wing types, the flexible wing's instantaneous peak thrust is much higher than that of the rigid wing, while its thrust trough is slightly lower than that of the rigid wing. For most of the cycle, the flexible wing's thrust is greater than that of the rigid wing. Comparing time-averaged thrust, as shown in Table 3, the flexible wing's time-averaged thrust is positive, while the rigid wing's time-averaged thrust is negative, indicating that flexible deformation has a dramatic effect on thrust performance.



(a)Lift comparison under identical conditions (b)Thrust comparison under identical conditions

Figure 15 – Comparison of lift and thrust between rigid and flexible wings.

Table 3 – Time-averaged lift and thrust of rigid and flexible wings.

Wing Type	Time-Averaged Lift	Time-Averaged Thrust
Rigid Wing	0.68N	-0.09N
Flexible Wing	0.52N	0.14N

4.2 Comparison of Pressure and Vortex Characteristics

Figure 16 shows the surface pressure contours on the upper and lower surfaces at the times of maximum downstroke and upstroke velocity. It can be seen that compared to the flexible wing, at the downstroke instant (t/T=0.25), the rigid wing has lower pressure on the upper surface and higher pressure on the lower surface, resulting in a larger pressure difference (positive lift). At the upstroke instant (t/T=0.75), the rigid wing has higher pressure on the upper surface and lower pressure on the lower surface, resulting in a larger pressure difference (negative lift).

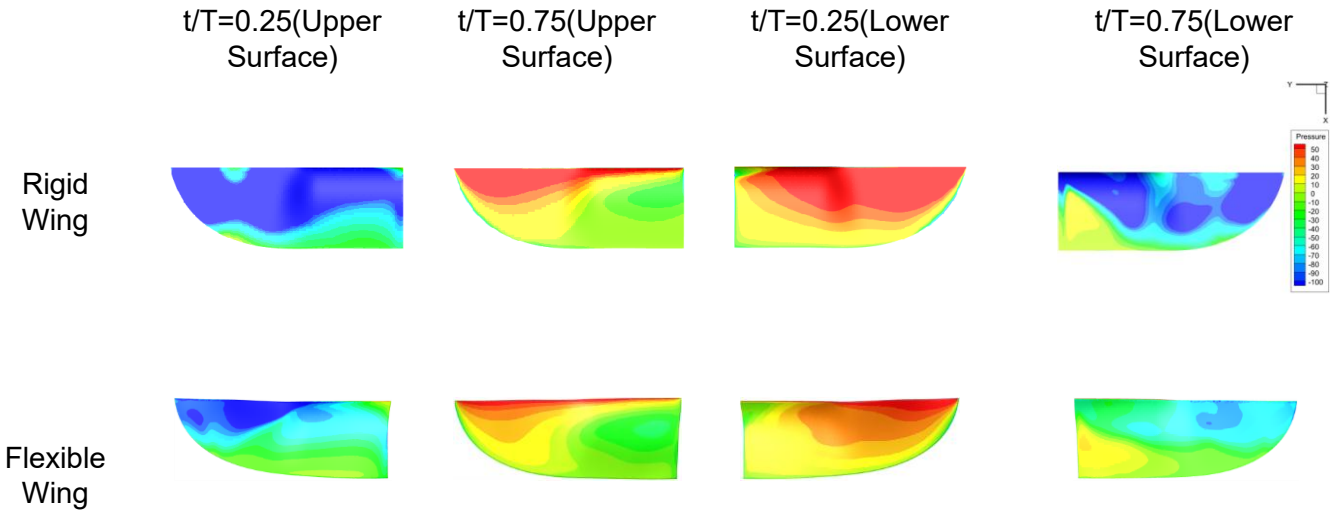


Figure 16 – Surface pressure contours of rigid and flexible wings at maximum downstroke (t/T=0.25) and maximum upstroke (t/T=0.75) velocity.

Figure 17 shows pressure contours on the same cross-section (approximately 0.18 times the semi-span from the wing root) at these instants. According to the figure, at the maximum downstroke instant (t/T=0.25), the rigid wing's low-pressure region on the upper surface is significantly larger than that of the flexible wing, and the pressure values are much lower than those of the flexible wing, hence its positive lift is also larger. At the maximum upstroke instant (t/T=0.75), the rigid wing's low-pressure region on the lower surface is significantly larger than that of the flexible wing, and the

pressure values are much lower than those of the flexible wing. The flexible wing exhibits a high-pressure region on the lower surface near the trailing edge, generating positive lift that counteracts some negative lift. Therefore, the rigid wing's negative lift is larger. This is consistent with the above conclusion.

Furthermore, observing the airfoil pitch angle reveals that at the maximum downstroke instant, the flexible wing is significantly nose-down relative to the rigid wing, i.e., the leading edge tilts downward. This indicates that the flexible wing undergoes downward twisting deformation during the downstroke. This downward twist reduces the effective angle of attack of the wing surface, causing the aerodynamic force generated by the pressure difference to tilt forward, thereby decomposing into a larger thrust component horizontally. At the maximum upstroke instant, the flexible wing is significantly nose-up relative to the rigid wing, i.e., the leading edge tilts upward. This indicates that the flexible wing undergoes upward twisting deformation during the upstroke. This upward twist increases the effective angle of attack. For the part near the leading edge, the pressure difference force tilts forward, contributing a thrust component horizontally. However, at this moment, the flexible wing also exhibits a high-pressure region on the lower surface near the trailing edge, causing the pressure difference force on the trailing edge section to tilt backward, contributing a drag component horizontally. After cancellation, the net thrust component is reduced. For the rigid wing, the region with significant pressure difference on the upper and lower surfaces at the maximum downstroke instant (t/T=0.25) is much larger than that at the maximum upstroke instant (t/T=0.75). Therefore, the drag of the rigid wing at the maximum downstroke instant is greater than its drag at the maximum upstroke instant, consistent with the above conclusion.

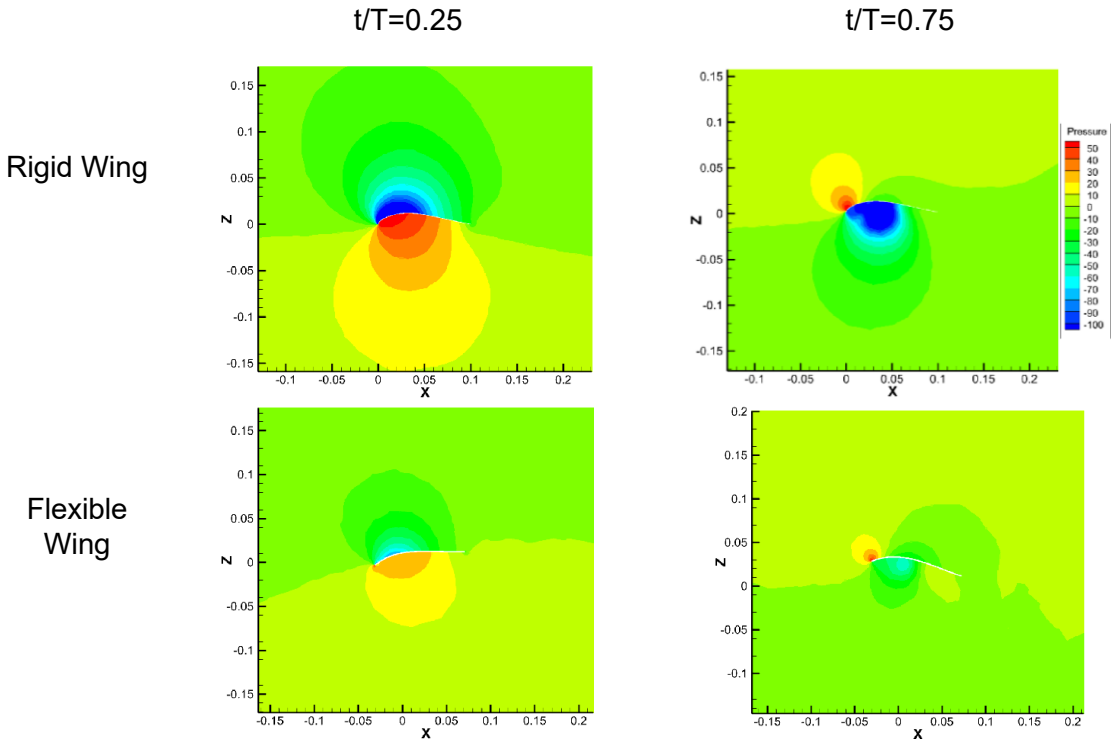


Figure 17 – Pressure contours on a typical cross-section of rigid and flexible wings at t/T=0.25 and t/T=0.75.

Figure 18 compares the iso-surfaces of Q-criterion (Q=10000) for the rigid and flexible wings at different times, including top views and front views.

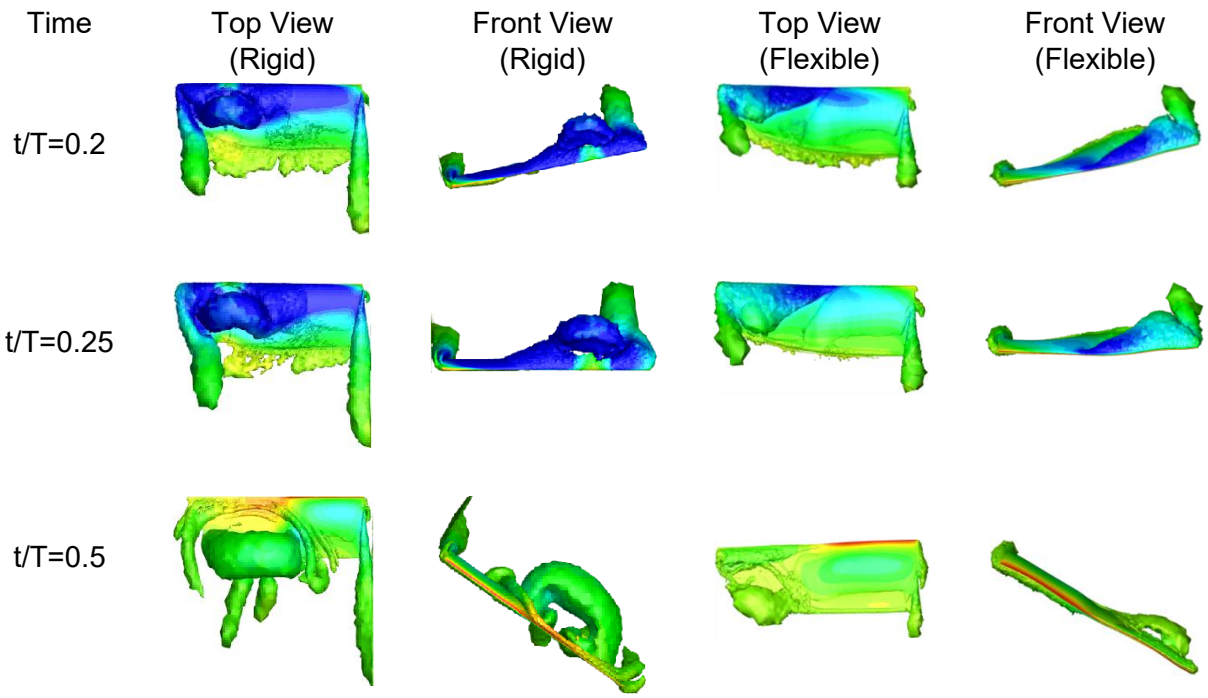
Rigid wing vortex evolution characteristics: Near the time of maximum downstroke velocity (t/T=0.2), a strong leading-edge vortex (LEV) forms and begins to show a tendency to detach from the wing surface. As downstroke velocity increases, the LEV gradually moves towards the trailing edge. At the maximum downstroke instant (t/T=0.25), the LEV intensity reaches its maximum, and more vortex detaches from the wing surface. Near the downstroke limit position (t/T=0.5), the LEV has mostly detached from the wing surface, forming a large-scale wake vortex structure. During the

upstroke, a similar process occurs on the lower surface of the wing, generating negative lift.

Flexible wing vortex evolution characteristics: Near the time of maximum downstroke velocity (t/T=0.2), an LEV forms on the flexible wing, with intensity slightly lower than that of the rigid wing. As flapping proceeds, the LEV generated on the hand-wing section (outer wing section) of the flexible wing does not detach as quickly as that of the rigid wing. Instead, it remains persistently attached to the wing surface and gradually moves towards the trailing edge. At the downstroke limit position (t/T=0.5), some vortex detaches, but a considerable portion of the LEV remains attached to the leading edge region of the hand-wing section, and the wake vortex intensity is relatively weaker. This maintains a low-pressure region in the hand-wing section area, generating positive lift, which explains why the flexible wing's lift shows a plateau or no decrease near the downstroke limit position.

The comparison reveals that for both wings, the LEV forms at the leading edge during downstroke, then gradually moves towards the trailing edge until detachment. Since the rigid wing generates stronger vortices on its surface, its lift is larger. From the front views, it can be observed that the wingtip vortex tilts towards the upper surface of the wing during downstroke and towards the lower surface during upstroke. Because the flexible wing's wingtip vortex intensity is relatively weaker, its induced drag is also smaller than that of the rigid wing.

Compared with the rigid wing, the most significant difference for the flexible wing lies in the attachment behavior of the LEV. When the LEV forms at the leading edge and moves backward during the downstroke, the rigid wing quickly exhibits LEV detachment from the wing surface, while the flexible wing's vortex remains attached to the surface for a longer duration. During this phase, the thrust generated by the flexible wing is significantly greater than that of the rigid wing, suggesting that the LEV is an important factor affecting thrust. At t/T=0.2 and t/T=0.7 (respectively near the maximum downstroke and upstroke velocity instants), the degree of LEV attachment and its intensity for the flexible wing are significantly stronger than at other times. These two instants correspond exactly to the two peak positions of the thrust curve. The vortex at t/T=0.2 is stronger than that at t/T=0.7, corresponding to the larger thrust peak during downstroke. This phenomenon clearly indicates that sustained attachment of the LEV is the key mechanism for the substantial thrust increase in the flexible wing.



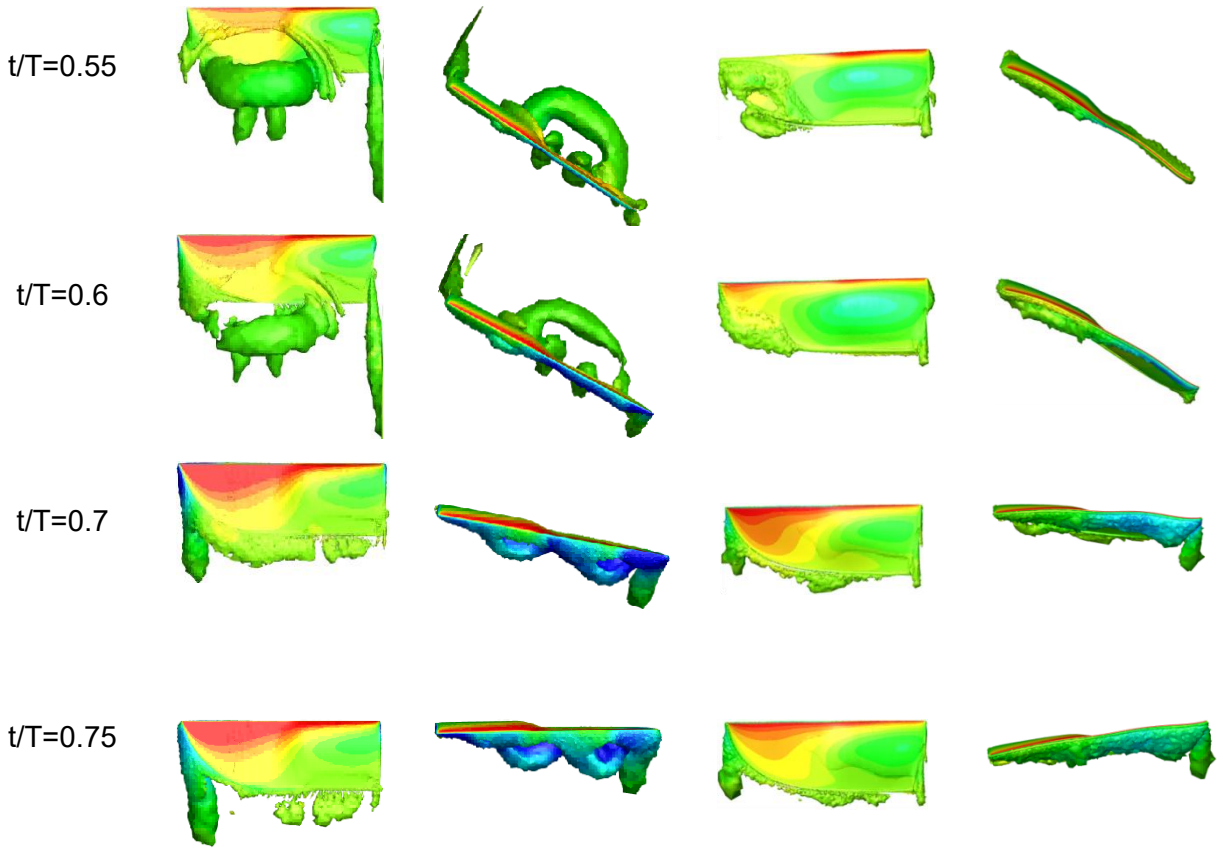


Figure 18 – Vortical structures (Q-criterion, Q=10000) of rigid and flexible wings at representative time instants.

4.3 Preliminary Analysis of Torsional Deformation and Aerodynamic Mechanism

To preliminarily analyze the deformation characteristics of the flexible wing, two cross-sections were selected (Section 1: line connecting points 6-15; Section 2: line connecting points 7-14). Using the wing root chord line (connecting points 5-16) as a reference, the twist angle of each cross-section relative to the wing root was calculated to observe wing surface twisting deformation. Nose-down twist (lowering) relative to the wing root is defined as positive. Based on the marker coordinate data, the twist angles of the cross-sections were calculated to preliminarily observe the deformation. Figure 19 shows the torsional deformation curves of the two sections over one cycle. It can be observed that the cross-section closer to the wing root (Section 1) exhibits smaller torsional deformation, while the cross-section closer to the wing tip (Section 2) exhibits larger torsional deformation, indicating that torsional deformation amplifies along the spanwise direction. Over one cycle, downward twist (positive angle) occurs during the downstroke, and upward twist (negative angle) occurs during the upstroke. Particularly near the two instants t/T=0.2 and t/T=0.7, the torsional deformation is largest, and the downward twist angle is larger than the upward twist angle. This directly corresponds to the phenomenon where the downstroke thrust peak is larger than the upstroke peak in the thrust curve.

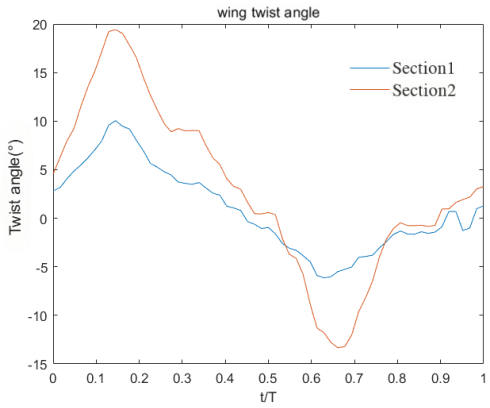


Figure 19 – Torsional deformation of different cross-sections of the flexible wing.

Based on this phenomenon, further analysis can be made. During the downstroke, the torsional deformation reduces the effective angle of attack, causing the vortices that were about to separate from the wing surface to reattach, delaying LEV separation, thus consistently generating larger thrust. From a theoretical perspective, both upward twist during upstroke and downward twist during downstroke cause the wing to push a large amount of air backward during flapping motion. According to Newton's third law, this reaction force is the source of thrust. Moreover, since the downward twist angle is larger than the upward twist angle, the projected area pushing air backward is also significantly larger during the downstroke than during the upstroke, corresponding to the significantly larger thrust peak during the downstroke.

5. Conclusion

This paper takes the 'Dove'-inspired flapping wing as the research object, comprehensively employs numerical simulation and high-speed photogrammetry methods, and investigates the effects of flexibility on the aerodynamic characteristics of the flapping wing. A CFD method for the flexible wing based on DIC-measured deformation is adopted, achieving accurate simulation of the dynamic deformation of the wing surface, and an in-depth comparison with the rigid wing is conducted. The main conclusions are as follows:

(1) Lift characteristics: Under identical experimental conditions, the time-averaged lift of the flexible wing (0.52 N) is lower than that of the rigid wing (0.68 N), a decrease of approximately 23.5%. Near the downstroke limit position, the flexible wing exhibits a unique phenomenon of plateauing or even slightly increasing lift due to the sustained attachment of the leading-edge vortex (LEV), whereas the lift of the rigid wing continuously decreases.

(2) Thrust characteristics: Flexibility fundamentally transforms thrust performance. The time-averaged thrust of the rigid wing is -0.09 N (net drag), while that of the flexible wing is 0.14 N (net thrust), a net increase of 0.23 N. The flexible wing generates two positive thrust peaks during the downstroke and upstroke, corresponding to the instants of maximum downward twist and maximum upward twist, respectively.

(3) Vortex characteristics: The sustained attachment of the LEV is the core mechanism for thrust enhancement in the flexible wing. The vorticity contours clearly show that the LEV of the flexible wing remains attached to the wing surface for the vast majority of the downstroke and upstroke, whereas the LEV of the rigid wing detaches rapidly. This difference leads to completely distinct lift and thrust performance between the rigid and flexible wings.

(4) Deformation mechanism: The flexible wing exhibits a passive twisting deformation pattern of "nose-down during downstroke, nose-up during upstroke" during flapping motion, and the torsional deformation amplifies along the spanwise direction. The torsional deformation during the downstroke reduces the effective angle of attack, causing the LEV to remain attached to the wing surface without detaching (though its intensity decreases). Consequently, the flexible wing experiences relatively reduced lift but increased thrust.

6. Contact Author Email Address

The contact author email address should appear explicitly in this section to facilitate future contacts.
ykr@mail.nwpu.edu.cn

7. Copyright Statement

The authors confirm that they, and/or their company or organization, hold copyright on all of the original material included in this paper. The authors also confirm that they have obtained permission, from the copyright holder of any third party material included in this paper, to publish it as part of their paper. The authors confirm that they give permission, or have obtained permission from the copyright holder of this paper, for the publication and distribution of this paper as part of the ICAS proceedings or as individual off-prints from the proceedings.

References

[1] Zhao Y P. Key problems of mechanics and smart materials in micro air vehicles (in Chinese) [J]. Science Foundation of China, 2000(01):13-16. DOI:10. 16262/j.cnki.1000-8217. 2000.01.004.

[2] Hedrick L T, Cheng B, Deng X. Wingbeat time and the scaling of passive rotational damping in flapping flight[J]. Science, 2009, 324(5924):252-255.

[3] Dornheim M A. Tiny drones may be soldier' s new tools[J]. Aviation Week & Space Technology, 1998, 148:42-43.

[4] Ashley S. Palm-size spy plane[J]. Mechanical Engineering, 1999, 120(2):74-78.

[5] Betteridge D S, Archer R D. A study of the mechanics of flapping wings[J]. Aeronautical Quarterly, 2016, 25(2):129-142.

[6] Hall K C, Pigott S A, Hall S R. Power requirements for large-amplitude flapping flight[J]. Journal of Aircraft, 2015, 35(3):352-361.

[7] Umberto P, Jane Z W. Flapping wing flight can save aerodynamic power compared to steady flight[J]. Physical Review Letters, 2009, 103(11):118102.

[8] Song B F, Lang X Y, Xue D, et al. A review of the research status and progress on the aerodynamic mechanism of bird wings (in Chinese). Sci Sin Tech, 2022, 52: 893–910, doi: 10.1360/SST-2020-0515

[9] Heathcote S, Gursul I. Flexible flapping airfoil propulsion at low Reynolds numbers[J]. AIAA Journal, 2007, 45(5):1066-1079.

[10] Heathcote S, Wang Z, Gursul I. Effect of spanwise flexibility on flapping wing propulsion[J]. Journal of Fluids and Structures, 2008, 24(2):183-199.

[11] Deng S, Percin M, Van O B W, et al. Numerical simulation of a flexible X-Wing flapping-wing micro air vehicle[J]. AIAA Journal, 2017, 55(7):2295-2306.

[12] Song J, Luo H, Hedrick T L. Three-dimensional flow and lift characteristics of a hovering ruby-throated hummingbird[J]. Journal of The Royal Society Interface, 2014, 11(98):20140541.

[13] Song J, Tobalske B W, Powers D R, et al. Three-dimensional simulation for fast forward flight of a calliope hummingbird[J]. Royal Society Open Science, 2016, 3(6):160230.

[14] Bode-Oke A T, Dong H. The reverse flight of a monarch butterfly (Danaus plexippus) is characterized by a weight-supporting upstroke and postural changes[J]. Journal of The Royal Society Interface, 2020, 17(167):20200268.

[15] Shumway N, Gabryszuk M, Laurence S. The impact of dragonfly wing deformations on aerodynamic performance during forward flight[J]. Bioinspiration & biomimetics, 2020, 15(2):26005.

[16] Yang W Q. Numerical simulation of flow around flapping-wing vehicle based on overset grid (in Chinese). Ph.D. Dissertation, Xi'an: Northwestern Polytechnical University, 2010.

[17] Chen L L, Research on aeroelastic coupling calculation and optimization design for micro flapping-wing (in Chinese). Ph.D. Dissertation, Xi'an: Northwestern Polytechnical University, 2013.

[18] Y Xiaowu, S Bifeng, Y Wenqing, et al. Study of aerodynamic and inertial forces of a dovelike flapping-wing MAV by combining experimental and numerical methods[J]. Chinese Journal of Aeronautics, 2022,35(6):63-76. DOI: 10.1016/J.CJA.2021.09.020.

[19] Liu H. Integrated modeling of insect flight: From morphology, kinematics to aerodynamics[J]. Journal of Computational Physics, 2009, 228(2):439-459.

[20] Lang X Y. Numerical simulation of three dimensional complex flow field characteristics of bird-like flapping wings (in Chinese). Dissertation, Xi'an: Northwestern Polytechnical University, 2019.

[21] Boer A, Schoot M S, Faculty H B. Mesh deformation based on radial basis function interpolation[J]. Computers and structures, 2007, 85(11): 784-795.